



A dynamics study of the A-chain of ricin by terahertz vibrational calculation and normal modes analysis

Hailiang Zhang, Eli Zukowski, Radhakrishnan Balu, Susan K. Gregurick*

Department of Chemistry and Biochemistry, University of Maryland, Baltimore County, 100 Hilltop Circle, Baltimore, MD 21250, United States

ARTICLE INFO

Article history:

Received 14 August 2008

Received in revised form 21 October 2008

Accepted 22 October 2008

Available online 30 October 2008

Keywords:

Ricin-A-chain

Depurination mechanism

CHARMM

Normal modes analysis

Terahertz spectroscopy

ABSTRACT

We studied the terahertz (THz) spectroscopy and low frequency normal modes of both apo- and holo- (adenosine monophosphate (AMP)-bound) ricin-A-chain (RTA) as a means to understand the dynamical changes that RTA undergoes upon substrate binding. The calculated THz spectra of apo- and holo-RTAs demonstrated a general intensity suppression upon substrate binding, which is attributed to the reduced number of collective motion in THz region. In normal mode analysis of RTA we find a shearing motion that is shared by both the apo- and holo-RTAs, whereas a breathing motion, and an upward hinge rising and an α -G bending characteristic motion are dampened significantly upon AMP binding, suggesting these motions are involved in the necessary flexibility of the active site. In contrast, we find a normal mode motion that separates domains I and II of RTA at the interface that is more common in the holo-protein. We hypothesized that the flexibility of the entrance of RTA can facilitate the entry of rRNA and allow the substrate to adjust its conformation and orientation *prior to* depurination. This process suggests an rRNA binding pathway which is supplemental the current RTA depurination mechanism.

Published by Elsevier B.V.

1. Introduction

Terahertz (THz) spectroscopy is an absorption spectroscopy that deals with the far infrared (IR) region (typically 0–100 cm^{-1}) of the electromagnetic spectrum. Specific examples of the use of high resolution THz spectroscopy to study and characterize single amino acids [1–5], crystalline peptides [6], proteins [7,8], nucleic acids [9–12], and explosives [13–15] points to the possibility for rapid and unambiguous identification of chemical agents, precursors, and degradation products. Moreover, since THz spectroscopy probes the molecular absorbance at the lowest frequency regime, this method is uniquely suited to investigate collective motions inherent in biological activation [16,17]. For example, it has been used to study and characterize the dynamical transition of cytochrome c, the dynamics of bacteriorhodopsin and mutants, the binding activity of lysozyme with 3NAG, the solution phase dynamics of nucleotides, the dynamics comparison between the native and thermally denatured bovine serum albumin (BSA), and the dynamics difference of photoactive yellow protein (PYP) between the pG (rigid) state and the pB (partial unfolded) state [7–8,18–24].

When considering protein dynamics and the pathways to conformational changes, the low frequency motions are thought to be pivotal, and THz region *normal modes analysis* has provided significant insights into structure–function relationships for biological systems [8,25–28]. For example, a comparison of low frequency normal mode motions and the directions of large-amplitude fluctuations from molecular dynamics simulations indicates clear similarities [29,30]. In particular, the calculated root-mean-square amplitudes of the atomic displacement from a normal mode analysis of bovine pancreatic trypsin inhibitor, compared against motions obtained from a molecular dynamics simulation based on the same potential energy function, suggested that a normal mode description can provide a reliable description of the internal motions of proteins [31,32]. Since normal modes analysis (NMA) of proteins is relatively straightforward, this method, combined with terahertz spectroscopic analysis of the lowest vibrational frequencies, offers a glimpse into the possible inherent dynamics of protein activation. However, as pointed out by Ma [33], the functionally important modes are usually a subset of these lower frequency normal modes and are often difficult to determine *a priori*. Nevertheless, by comparing the apo- against the holo-protein's normal mode spectra, one can determine changes in the characteristic motions that illustrate ligand-induced conformational transitions [33]. Therefore in present research, we have studied the low frequency THz spectroscopy of both apo- and holo- (adenosine monopho-

* Corresponding author. Tel.: +1 301 903 7672; fax: +1 301 903 0567.

E-mail address: greguric@umbc.edu (S.K. Gregurick).

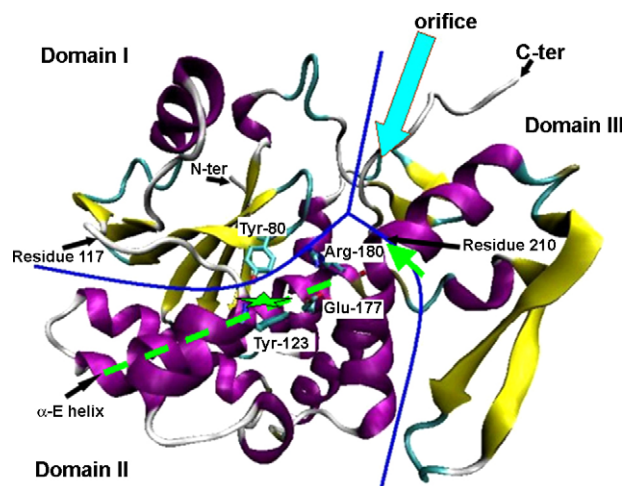


Fig. 1. Ribbon representation of RTA crystal structure (PDB ID: 1IFT) using VMD [54] that is colored by secondary structural features—purple for α -helices and yellow for β -sheets. The blue lines outline the interfaces between domains I, II and III. The position of N-terminal and C-terminal, as well as some residues bordering between domains, are marked with black arrows. The turquoise arrow on the top demonstrates the orifice of RTA through which the substrate enters. The green star in the middle demonstrates the binding site of adenine ring. The green arrow on the right indicates the position of residue 210 where α -G helix is bent into α -G1 and α -G2. The green dashed line demonstrates α -E helix, or the “hinge” of the “breathing” motion in the normal modes analysis.

sphate (AMP)-bound) ricin-A-chain (RTA) as a means to understand the dynamical changes of ricin-A-chain upon substrate binding.

Ricin is an extraordinary cytotoxic protein which is isolated from the seeds of *Ricinus communis* (castor beans) and is among the most lethal proteins. Ricin will catalytically hydrolyze the N-glycosidic bond of a specific adenosine in 80S ribosomal RNA, thus inhibiting protein synthesis in eukaryotic cells. Structurally, ricin is composed of two subunits, ricin-A-chain and ricin-B-chain (RTB) that are linked by a single disulfide bond. RTB is a galactose binding lectin which binds the glycoproteins or glycolipids on the cell membrane and facilitates easy entry of the protein into the cell. Once inside the cell, the disulfide bond between RTA and RTB is reduced and RTA is translocated into the cytoplasm across an internal membrane. Thereafter, RTA will attack and depurinate an invariable GAGA tetraloop of ribosomal RNA and inhibit protein synthesis.

RTA is a globular protein that is composed of 267 residues. The X-ray crystallographic structures of RTAs were obtained with a

resolution of up to 1.8 Å [34–36]. Figs. 1 and 2 demonstrate the structure and structural features of RTA. Overall, RTA can be divided into three subdomains [37]. Domain I, the N-terminal domain (residue 1–117), is composed of two parallel $\beta\alpha\beta$ units (β -A, α -A, β -B and β -E, α -B, β -F) separated by an anti-parallel β -strand (β -C, β -D). Domain II, the middle domain (residue 118–210), is comprised of five α helices (α -C, α -D, α -E, α -F and α -G1). It has been found that this domain contains a series of highly conserved residues that have been proposed to be crucial for substrate binding and depurination (e.g. Tyr-123, Glu-177, and Arg-180). Domain III, the C-terminal domain (residues 210–267), consists of two anti-parallel β -strands (β -G and β -H) and a partial helical structure (α -G2); the interface between RTA and RTB is located on this domain. We note that the last α helix of domain II (α -G1) and the first α -helix of domain III (α -G2) form a unified helix (α -G) which is bent at residue 210.

The active site of RTA is located in a cleft that is formed between the three domains. A mechanism for substrate binding and depurination has been proposed based on structural and kinetics analysis and mutagenesis studies of RTA (Fig. 3) [38–40]. Briefly, the mechanism is proposed as follows: After entering the cleft of RTA, the adenine plane of rRNA is sandwiched between the phenol planes of Tyr-80 (located in domain I) and Tyr-123 (located in domain II) by forming a π stacking interaction. Then, aided by protonation by Arg-180 and stabilization by Glu-177, the N-glycosidic bond is cleaved and the adenine ring is released. This mechanism was hypothesized based on the X-ray crystallographic structure of RTA bound with mono- or di-nucleotide substrate analogs such as formycin monophosphate (FMP) [39]. However, although the FMP–RTA complex has been argued to be a transition state analog for the N-glycosidic reaction [41], previous experiments performed by Monzingo and Robertus have found that FMP is actually not an inhibitor of RTA [39]. Instead, it is believed that a double-helical stem of at least three base pairs in length is essential for detectable activity [42]. Unfortunately, to the best of our knowledge, there is now no experimental structure available for RTA bound with a native substrate or a substrate analog with a comparable size.

Given our current understanding of the ricin structure and mechanism, persistent questions still remain as to how the rRNA enters into the cleft and is trapped in the sandwiched structure. For example, based on the proposed mechanism, after entering the cleft, the adenine plane of the rRNA will be sandwiched between the two phenol rings (Tyr-80 and Tyr-123) of RTA; however, according to the crystal structure of the sarcin/ricin loop from rat 28S rRNA (PDB ID: 430D) [43] the target adenine plane of rRNA (Ade-15) is originally stacked parallel to its adjacent guanine plane

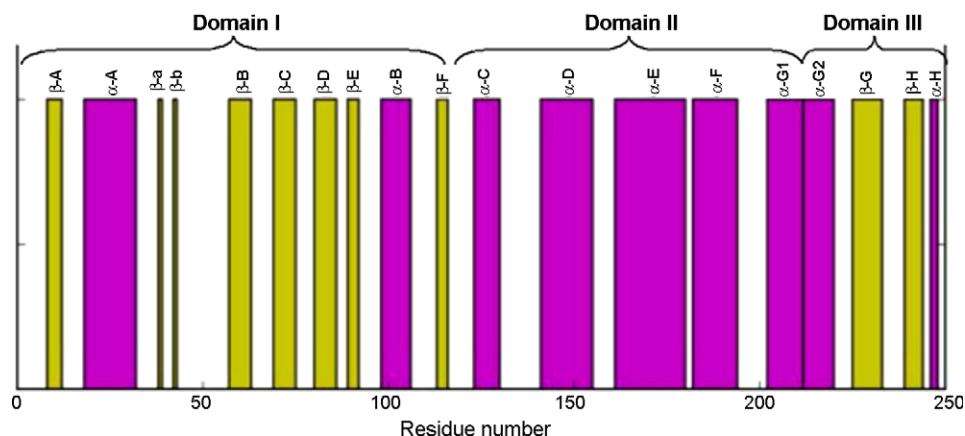


Fig. 2. The secondary structure distribution from the RTA crystal structure (PDB ID: 1IFT): pink for α -helices and yellow for β -sheets.

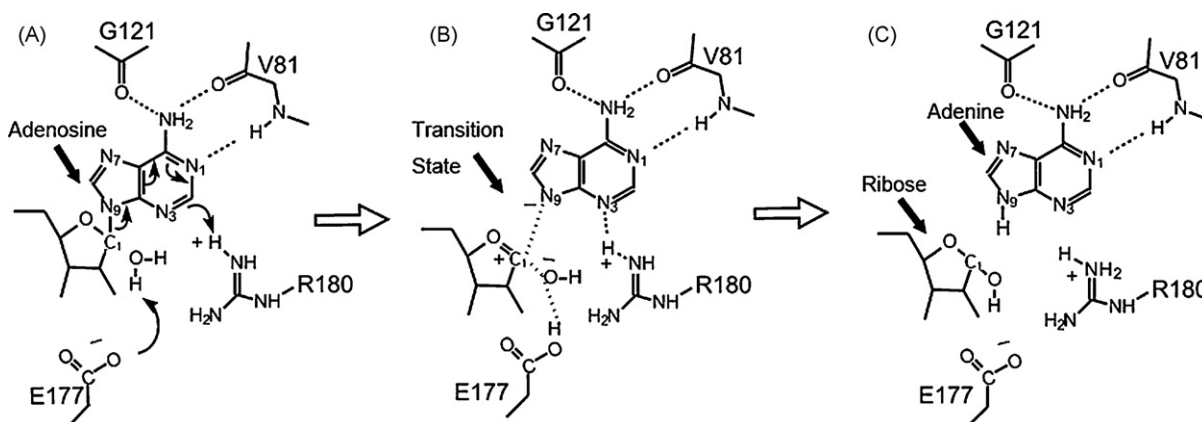


Fig. 3. (Courtesy of Dr. Jon Robertus, University of Texas) The mechanism of action for RTA. (a) Adenosine binds in the RTA active site. It stacks with the aromatic side chains of tyrosines 80 and 123 lying above and below the plane of the paper. Specific hydrogen bonds are formed from the RTA backbone to the adenine ring as indicated by the dotted lines. (b) The bond between adenine N9 and ribose C1 is cleaved, aided by protonation of N3 by Arg-180. An oxycarbonium ion forms on ribose as the bond is broken, and this is stabilized by ion pairing to Glu-177 via activating a bridged water molecule. (c) The activated water attacks the oxycarbonium, releasing the adenine leaving group.

(Gua-16). This implies that the position of the original guanine plane (Gua-16) of rRNA must be displaced by Tyr-80 of RTA upon substrate binding. This displacement process requires a realignment involving the adenine ring of Ade-15 and/or the main body of rRNA after entering the cleft. Yet the cleft size of RTA does not appear to be large enough for the native substrate to freely adjust its posture once inside the active site; we have confirmed this by modeling the Heus rRNA hairpin structure [44] into the active site of RTA. Therefore, the entire cleft of RTA must undergo a conformational change that allows rRNA to adjust its conformation and orientation in order to form the sandwich structure. One possible situation would be that the entrance is *flexible*. With a flexible entrance, rRNA can easily enter the cleft and realign the adenine ring in accordance to the two phenol rings.

NMA has been successfully employed to investigate large-scale fluctuations and overall flexibility of biological molecules [29,31,45,46]. The advantage of using a normal modes analysis is that individual motions and corresponding frequencies can be investigated very efficiently. Therefore this paper investigates the normal modes analysis of apo- and holo-RTA (bound with AMP) to reveal the flexibility of the protein in detail and to propose a dynamical mechanism of rRNA binding that is supplemental to the current depurination mechanism. Moreover, we also provide the distinctive THz spectra of both apo- and holo-RTAs as a means to study the changing dynamics in these two protein structures. This work focuses not only on the gas phase spectroscopy of RTA but also on the spectroscopy of the protein in a condensed, crystalline state. To the best of our knowledge, this is the first such calculation of the vibrational spectroscopy of proteins in a condensed, crystalline phase.

2. Methods

A single apo-RTA molecule is composed of 267 residues or over 2000 atoms. Given this large system size, the all-atom modeling based on aqueous solution is computational intractable, and hence the present THz vibrational calculation and normal modes analysis were carried out only under gas and crystalline conditions. Under these conditions, both the molecular structure and dynamical property may inevitably deviate from the aqueous condition to a certain extent. Nevertheless, we still expect our results under these limited conditions to yield insight into the RTA binding pathway due to the following justification: The structure of numerous proteins, including RTA, can be decomposed into several relatively

rigid subdomains. The low frequency modes in THz region are generally dominated by the soft and global inter-subdomain collective motions, in which the hard and detailed solvent–residue interactions under aqueous condition are relatively less important [29–33]. Based on this, we expect the present vibrational calculation and normal modes analysis under gas and crystalline conditions to shed light upon the dynamical pathway of RTA upon substrate binding. An exciting research on the dynamical coupling-incorporated vibrational calculations of large biological systems is currently underway.

The present THz vibrational calculations were carried out for apo- and holo-RTA (bound with AMP) under both gas phase and crystalline states. The initial structure of apo-RTA was obtained from Weson's X-ray crystal structure of recombinant RTA (PDB ID: 1IFT; mutation: I1M, F2V) [36], whereas that of the holo-RTA was obtained from Day's X-ray crystal structure of RTA bound with AMP (PDB ID: 1OBT; mutation: R180H) [47]. The former structure has a resolution of 1.8 Å, whereas the latter structure was resolved at 2.8 Å. The calculation of the THz vibrational spectra and normal modes analysis for the RTA proteins were accomplished using CHARMM version-c31b1 [48]. The original PDB structures, with all the crystallographic water molecules removed for the sake of computational expense, were read into the CHARMM data structure, and the hydrogen atoms were built automatically. The gas phase structures were obtained by minimizing a single PDB structure with 1000 steps of steepest descent algorithm, followed by 20,000 steps of Newton Raphson method until the gradient of the energy was within 0.00001 kcal/mol Å. The crystalline phase calculations on the RTAs were accomplished by constructing tetragonal crystal unit cells with dimensions of 68.700 Å × 68.700 Å × 141.500 Å for 1IFT.pdb and 68.65 Å × 68.65 Å × 141.10 Å for 1OBT.pdb. Similar to Day's method, only wavevector $k = 0$ was considered [49]. The periodic crystalline systems were maintained in our calculations by using periodic boundary conditions and Ewald summation methods. The crystalline protein systems were then energy minimized with 1000 steps of a steepest descent algorithm, followed by 100,000 steps of a Newton Raphson method until the gradient was within 0.0001 kcal/mol Å.

After energy minimization, the mass-weighted Hessian matrix was obtained for each system and the diagonalization of Hessian matrix produced the harmonic normal mode frequencies and motions. As a result, for apo-RTA under gas phase condition, the lowest frequency obtained was -0.002 cm^{-1} , while for apo-RTA under crystal phase condition, the lowest frequency obtained was

2.35 cm^{-1} . Similarly, for holo-RTA, the lowest frequency obtained was -0.002 cm^{-1} for gas phase and 2.86 cm^{-1} for crystal phase, respectively. These nearly zero lowest frequencies under gas phase conditions indicate that the gas phase structures were sufficiently energy minimized to produce stable local/global minimum. However, under crystal phase minimization, the positive frequencies (2.35 cm^{-1} and 2.86 cm^{-1}) could be partially due to the inter-lattice constraints and periodic boundary conditions which make it difficult to completely separate the rotational/translational degrees of freedom from the vibrational degrees of freedom. This was evident by investigating the vector representations of the first six normal modes in the crystal phase calculations (not shown), which were translational/rotational motions mixed with small amount of vibrational motions.

The intensity of the vibrational fundamental, $\nu' = \nu'' + 1$, of each normal mode, Q_i , is proportional to the square of the transition dipole moment derivative, $\delta\mu_i/\delta Q_i$, and is numerically evaluated according to [1,6]:

$$I_i \propto \left| \left\langle \nu' \left| \frac{\partial \mu_i}{\partial Q_i} \right| \nu'' \right\rangle \right|^2 \cong \left| \sum_j \frac{e_j q_{i,j} - e_j^0 q_{i,j}^0}{\Delta Q_i} \right|^2 \cong \left| \sum_j \frac{e_j^0 (q_{i,j} - q_{i,j}^0)}{\Delta Q_i} \right|^2 \quad (1)$$

where the sum is over all $3N$ Cartesian coordinate displacements, $q_j - q_j^0$, derived from the eigenvectors of the Hessian by dividing by square-root of the atomic masses, and ΔQ_i represents the root-mean-square displacement of atoms in mode Q_i , arbitrarily set to one in the final approximation of Eq. (1). Since CHARMM assigns a static partial charge, e_j^0 , according to atom type regardless of bond length, the electrical anharmonicity is by definition zero making the latter approximation necessary. Eq. (1) yields the integrated intensity and therefore, for comparisons with experiment, we have used a Lorentzian function to describe each line shape, as given by the following formula:

$$I(\nu_i) = \frac{I_{\max} \Gamma^2}{\pi[(\nu - \nu_i)^2 + \Gamma^2]} \quad (2)$$

In this case the lines are uniformly broadened at a temperature of 4 K where Γ is defined as the full width at half max (FWHM). Note that our frequency calculations are strictly at the harmonic level, and all lines are uniformly broadened at the harmonic level of theory.

Table 1

The RMSD of the energy-minimized RTAs from their starting PDB structures.

Phase	Apo-RTA	Holo-RTA
Gas phase	1.34	1.46
Crystal phase	1.45	1.92

Automatic alignments were performed using VMD-1.8.5 before RMSD calculations. All values are in units of Å.

3. Results and discussion

3.1. Structural changes of RTAs upon energy minimization

After energy minimization, a series of structural changes were observed for both the apo- and holo-RTAs. The RMSD (root-mean-square deviation) of the minimized structures from their starting PDB structures are shown in Table 1, and the changes of secondary structures upon energy minimization are illustrated in Fig. 4. Table 1 indicates that all RTAs have experienced structural changes after energy minimization and generally, the crystal phase minimization has led to larger structural deviations compared to the gas phase minimization. Because the water molecules have been removed to release the computational burden, the unit cell has shrunk slightly and this may produce larger lattice interactions in the crystal phase. This most likely accounts for the larger structural deviations found in the crystal phase.

Despite the RMSD differences, Fig. 4 reveals a similar structural change pattern between the gas and crystal phase minimizations. Overall we find that several loops around the cleft orifice have shrunk inward. These loops include the loop linking β -b/ β -B (residues 46–54, loop A), the loop linking β -E/ α -B (residues 94–98, loop B) and the loop linking β -F/ α -C (residues 118–123, loop C) (indicated by the arrows in Fig. 4). This may be due to the formation of hydrogen bonding and electrostatic interaction between Arg-48 and Asp-96 upon the removal of water. Fig. 5 demonstrates that the distance between Arg-48 and Asp-96 has decreased significantly upon energy minimization and consequently loops A and B have moved toward each other. Moreover, Fig. 4 also reveals that loop C tended to move upward along with loop B, which is possibly due to a series of hydrophobic and aromatic interactions between these two loops. This upward

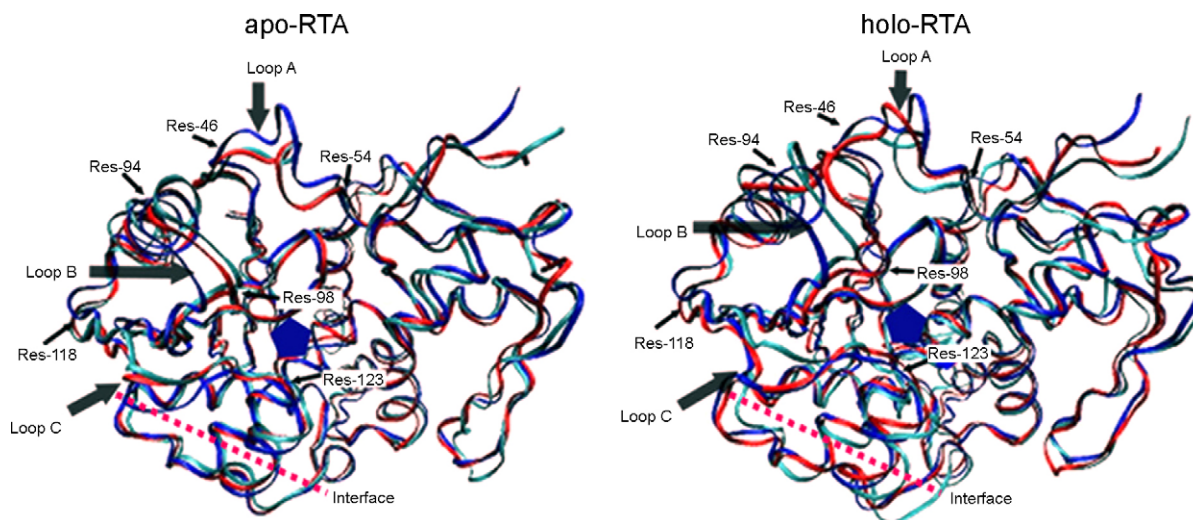


Fig. 4. The structural changes of apo-RTA (left) and holo-RTA (right) upon energy minimization. The original PDB structures are shown in blue, the minimized gas phase structures in red, and the minimized crystal phase structures in cyan. The thick arrows represent the three loops that experienced large structural changes upon energy minimization, and those residues bordering these loops are also marked. The blue pentagons represent the substrate binding sites of RTAs. The pink dotted lines represent the interfaces between domains I and II.

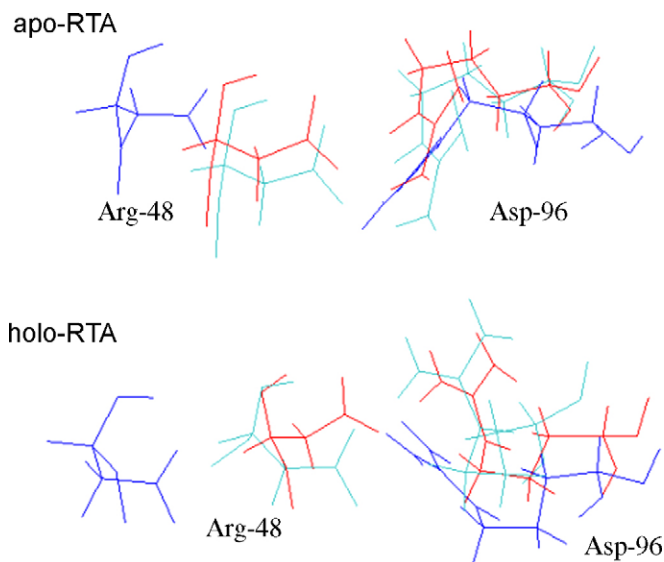


Fig. 5. The distance changes between Arg-48 and Asp-96 upon energy minimization for apo-RTA (upper) and holo-RTA (lower). The original PDB structures are shown in blue, the minimized gas phase structures in red, and the minimized crystal phase structures in cyan.

movement of loop C in Fig. 4 has an interesting effect on the interface structure between domains I and II that is located below this loop (indicated by the dashed lines in Fig. 4). This interface contains a series of aromatic residues (residue 80, 84, 91–94, 108, 115, 117, 119, 123, 152–154, 168), most of which pack parallel to each other except for certain residues such as Phe-119. Fig. 6 indicates that the upward moving of loop C upon energy minimization has improved the aromatic geometry of Phe-119 significantly and the interface structure is thus more stabilized. However, this situation was not reproduced in the gas phase-minimized holo-RTA, and as a result, the interface structure in holo-RTA was less stabilized and domains I and II tended to separate in the low frequency region as will be shown in the normal modes analysis.

3.2. Terahertz spectra of RTAs

The calculated terahertz spectra of RTAs minimized in the gas and crystal phase are shown in Fig. 7(A) and (B) respectively. The

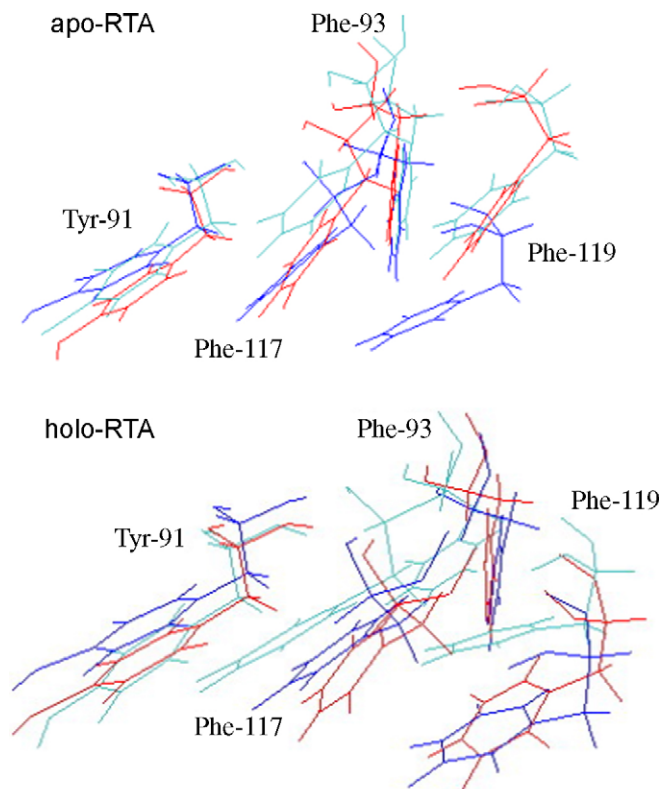


Fig. 6. The geometry change of Phe-119 in apo-RTA (upper) and holo-RTA (lower) upon energy minimization. The original PDB structures are shown in blue, the minimized gas phase structures in red, and the minimized crystal phase structures in cyan.

line shape of each mode was uniformly broadened using Lorentzian function at a temperature of 4 K (see Section 2 for details), at which the high-resolution THz spectrum is anticipated for large biological systems. Unfortunately, there is currently no experimental spectrum of RTA available at this resolution; however, based on our recent THz spectra study of rhodopsin and bacterhodopsin [18], we do expect that the calculated spectra will be comparable to the experiments at least from the overall trend. Moreover, comparison of the calculated spectra between the apo- and holo-systems still provides us with useful information

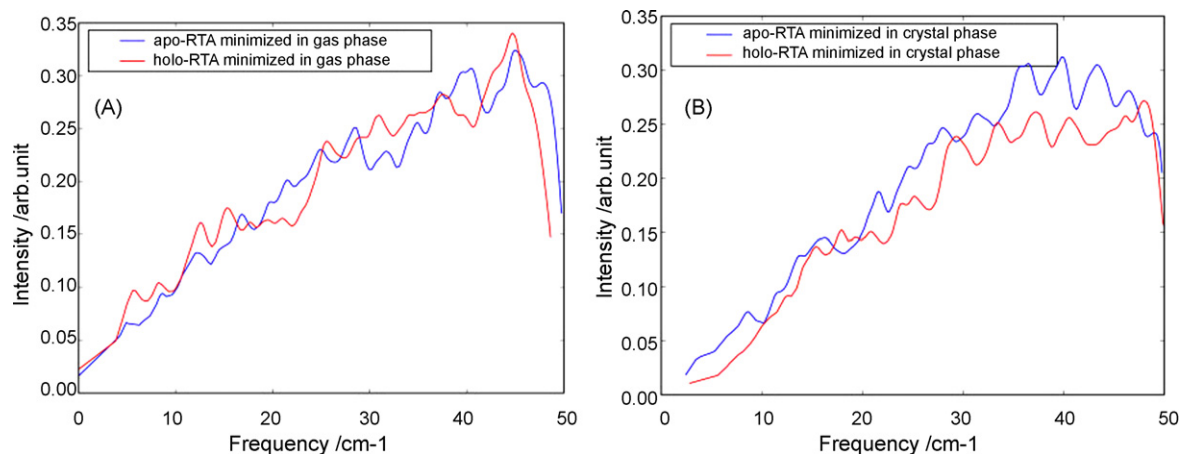


Fig. 7. The calculated terahertz spectra of the RTAs minimized in gas and crystal phase. (A) Comparison between apo- and holo-RTAs that are minimized in gas phase; (B) comparison between apo- and holo-RTAs that are minimized in crystal phase. As used by most references of VSCF calculations, “arbitrary unit” was used as the intensity of calculated spectra [57].

Table 2

The lowest 18 frequencies of RTAs calculated by CHARMM.

Normal mode	Apo-RTA-gas		Apo-RTA-cry		Holo-RTA-gas		Holo-RTA-cry	
	Frequency (cm ⁻¹)	T/R (%) ^a	Frequency (cm ⁻¹)	T/R (%) ^a	Frequency (cm ⁻¹)	T/R (%) ^a	Frequency (cm ⁻¹)	T/R (%) ^a
1	−0.00	100	2.35	92.85	−0.00	100	2.86	92.09
2	−0.00	100	3.66	72.67	−0.00	100	5.61	60.77
3	−0.00	100	4.82	73.57	0.00	100	6.56	64.56
4	0.00	100	5.18	80.42	0.00	100	6.84	58.81
5	0.00	100	5.81	43.44	0.00	100	7.68	25.86
6	0.00	100	7.10	35.94	0.00	100	8.14	11.53
7	4.23	0	7.31	8.24	3.82	0	8.85	22.90
8	4.89	0	7.52	18.47	4.55	0	9.31	20.49
9	5.23	0	8.08	5.25	4.98	0	10.00	18.99
10	6.28	0	8.56	8.73	5.55	0	10.28	4.92
11	6.43	0	8.78	16.10	5.85	0	10.77	7.17
12	6.76	0	9.17	10.92	6.12	0	10.94	2.48
13	7.36	0	9.90	4.14	6.52	0	11.48	15.56
14	8.03	0	10.41	5.17	6.81	0	12.12	1.69
15	8.32	0	10.84	2.85	7.11	0	12.24	2.02
16	8.53	0	11.08	0.98	7.55	0	12.41	4.91
17	8.68	0	11.16	2.52	8.06	0	12.70	4.93
18	9.04	0	11.45	4.65	8.13	0	12.92	3.75

^a The percentage of translational and rotational freedom in each normal mode.

about the structural dynamics of RTA upon substrate binding. For example, a notable difference is that the intensity of the holo-system is slightly reduced compared with the apo-system, which include almost the whole 0–50 cm⁻¹ region of the crystalline systems and the 20–25 cm⁻¹ and 38–42 cm⁻¹ region of the gas phase systems. The similar phenomena has been observed in other systems, for example in the binding measurement of lysozyme with 3NAG and solution phase measurements of nucleotides [20,21], in which the suppression of the frequency response in the bound systems was attributed to the suppression of structural flexibility with binding of a substrate. In a more recent THz spectroscopy study of PYP [23], a clear intensity decrease was observed in the pG (rigid) state PYP compared to the pB (partial unfolded) state, and this decreased intensity was contributed to a decrease in number of the delocalized normal modes of the rigid state compared to the flexible state. Correspondingly, in present research, we found that there were 307 normal modes in apo-RTA compared to 268 normal modes in holo-RTA between 0 and 50 cm⁻¹ under crystalline condition, which confirms that the intensity suppression of crystalline RTA upon substrate binding does accompany the decreased number of normal modes. However, probably due to lack of boundary constraints and lattice interactions, this intensity suppression was only observed between 20–25 cm⁻¹ and 38–42 cm⁻¹ for the gas phase-minimized RTAs, and correspondingly, we found there were 85 normal modes in apo-RTA compared to 79 normal modes in holo-RTA within these regions.

3.3. Normal modes analysis of RTAs

Based on classical mechanics, the amplitude of a given normal mode is inversely proportional to the corresponding frequency given a certain temperature [50,51]. The lower the frequency of a normal mode, the larger the amplitude and thus the larger the contribution to the overall motion. Specific examples of the analysis of low frequency motion and the contribution of normal modes to functional dynamics include hexokinase [52], lysozyme and BPTI [31,53], and citrate synthase [54]. In those examples only several lowest frequency modes were used to correlate with known protein function. Based on this, in the present work, we have studied the first 18 normal modes of apo- and holo-RTAs in detail in order to understand the collective motions of RTA.

The frequencies of the first 18 normal modes of RTAs are shown in Table 2; the percentages of translational and rotational (T/R) degrees of freedom of each normal mode are also listed. The percentage of T/R degrees of freedom was calculated by CHARMM based on the dot product between each normal mode with a pre-defined pure translational/rotational mode set. A 0% of T/R indicates a pure vibrational mode without displacement of center of mass or angular momentum with respect to the translating-rotating coordinate system. For a fully minimized system with no constraints, it can be proved that the first six modes upon Hessian diagonalization will correspond to pure T/R degrees of freedom with 0 frequencies [51]. In present study, for the RTAs minimized in the gas phase, the first six lowest frequencies are all approximately 0 cm⁻¹ and all are 100% pure T/R degrees of freedom. This indicates that the global/local energy minimums had been reached by the CHARMM energy optimization and therefore the following normal modes analysis will start from mode number 7. However, for the crystal phase-minimized RTAs, as described previously, the corresponding frequencies all start from positive non-zero values and the first six modes are mixed by certain amount of vibrational degree of freedom. Correspondingly, the following modes (numbers 7–18) are mixed by up to 22% by T/R degrees of freedom, which makes the vibrational motions more disordered and less tractable. Thus, no attempt was made to further analyze the normal mode motion of the crystal phase-minimized RTAs.

In order to better visualize the collective low frequency normal mode motions, a vector field representation was used for the selected vibrational frequencies. This method is similar to that of Thomas in that a vector field is calculated over a partition of the protein [55]. However, in our method, the protein was partitioned at each amino acid instead of on a cubic lattice. In the present research, the center of each amino acid partition was defined to be the C α carbon and all atomic displacement within a 4 Å radius were translated to this position. An overall vector field for each C α carbon was then calculated through vector addition of each composite atomic motion. The program to perform this work is written in Perl and is designed to interface with the visual molecular dynamics program VMD [56]. In the present paper, only those motions which were suspected to be related to the functions of interest, such as the flexibility of entrance as discussed in introduction, are listed in Fig. 8. Readers are encouraged to visit

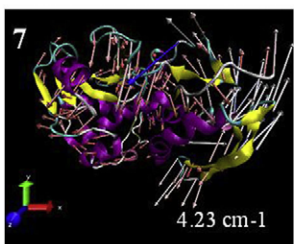
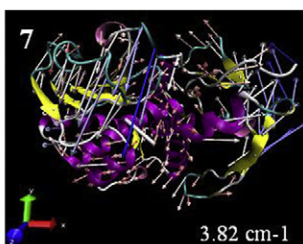
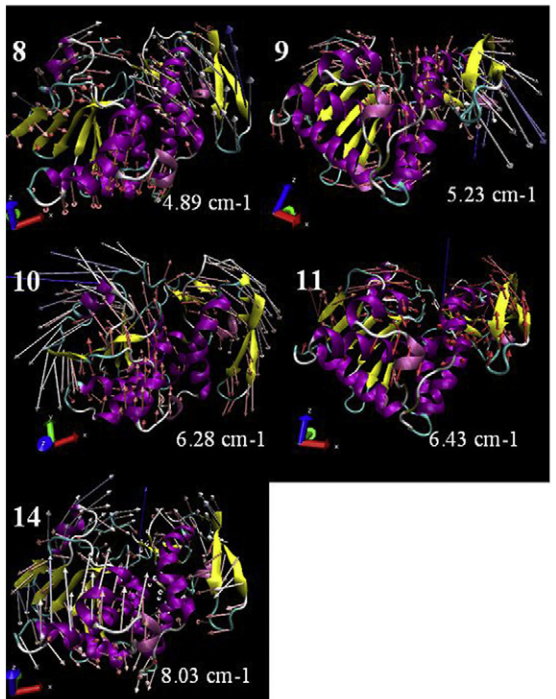
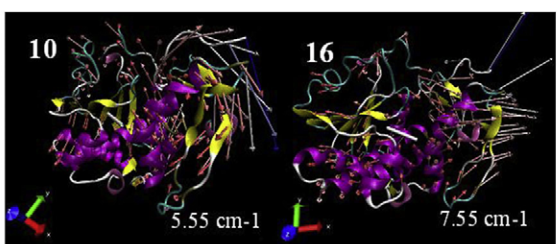
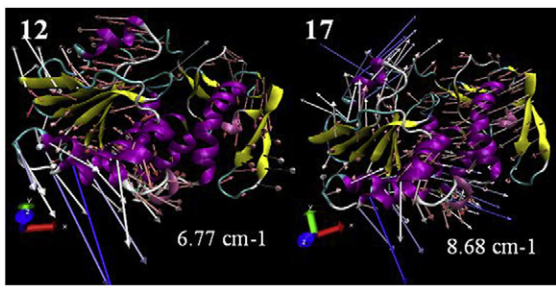
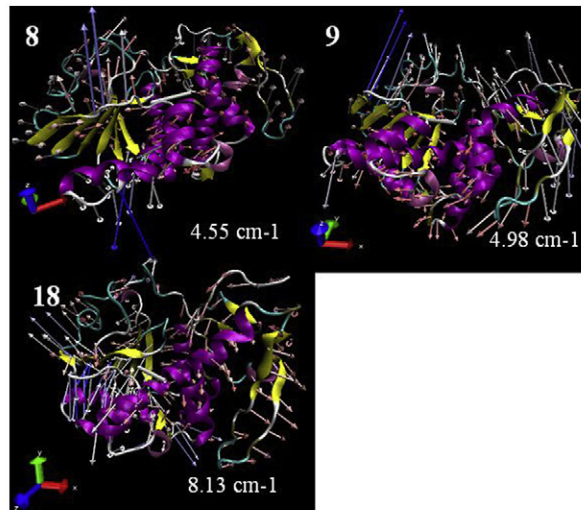
Shearing motion	<p>apo-RTA</p>  <p>7 4.23 cm⁻¹</p>	<p>holo-RTA</p>  <p>7 3.82 cm⁻¹</p>
Breathing motion	 <p>8 4.89 cm⁻¹ 9 5.23 cm⁻¹ 10 6.28 cm⁻¹ 11 6.43 cm⁻¹ 14 8.03 cm⁻¹</p>	 <p>10 5.55 cm⁻¹ 16 7.55 cm⁻¹</p>
Seperating domains I and II	 <p>12 6.77 cm⁻¹ 17 8.68 cm⁻¹</p>	 <p>8 4.55 cm⁻¹ 9 4.98 cm⁻¹ 18 8.13 cm⁻¹</p>

Fig. 8. Selected normal modes representation of RTAs minimized in gas phase. Normal mode numbers are shown at the upper-left corner of each mode, and the corresponding frequencies are shown at the lower-right corner. The orientation of each mode has been arranged from the best perspective in order to comprehend each specific motion. Note that the Cartesian coordinate axis at the lower-left corner of each mode may be used as a reference between different modes: the “+z” direction (blue) is approximately pointed from the active site toward the cleft entrance; the “-x” direction (red) is approximately pointed from the active site toward domain I; and “+x” direction (red) is approximately pointed from the active site toward domain III.

<http://userpages.umbc.edu/~zhangh1/Ricin/> for the animations of all the normal modes.

3.3.1.1. Apo-RTA in gas phase

Investigation of the vector field representations of gas phase-minimized apo-RTA indicated that most of the low frequency modes represent specific collective motions between domains I, II and III. For example, the lowest vibrational mode, mode 7 (4.23 cm^{-1}) of apo-RTA reveals that domains I/II (as a whole) and domain III vibrates along opposite directions (Fig. 8) (except for a small area between β -G and β -H). This motion is designated as a “shearing” motion in the present research. A closer investigation reveals that the vibrational direction is reversed at residue 210. As discussed in the introduction, this residue bends the α -G helix and divided the helix into two subunits: α -G1 and α -G2 (Fig. 1). The reversal of the vibrational direction at residue 210 will further bend the α -G helix (termed here as “ α -G bending” characteristic motion). Since the α -G2 helix constitutes one side of the rRNA entrance (Fig. 1), this α -G bending characteristic motion further facilitates the entry of rRNA into the cleft.

The following normal modes 8–11 (4.89 – 6.43 cm^{-1}) are dominated by a different type of collective motion, where domains I and III separate while domain II tends to move upward toward the orifice (Fig. 8). We designate this motion as a “breathing” motion among domains I, II and III. The hinge of this motion can be located on the α -E helix in domain II (Fig. 1), which contains a series of highly conserved residues (Glu-177 and Arg-180) responsible for substrate binding and hydrolysis. Notably, the hinge is not stationary but actually moves upward toward the orifice along with domain II when domains I and III are separated (termed here as “upward hinge” characteristic motion). We hypothesize that the upward hinge characteristic motion exposes the active site to the solvent environment and thus it is more ready to accept substrate. Moreover, the α -G bending characteristic motion is also found in most of the breathing-like motions (modes 8–10, 14). We note that these characteristic motions are absent in many of the normal modes of holo-RTA.

The remainder of the low frequency normal modes of apo-RTA tended to be less collective and thus less tractable, and were characterized by more disordered vibrational directions and an unequally distribution of vibrational amplitudes. In general the highest vibrational amplitudes for most of these modes were localized around the terminal regions or flexible loops, with the exception of modes 12 and 17, where domains I and II tended to separate at the interface. This specific motion will be discussed more in the following normal modes analysis of holo-RTA.

3.3.1.2. Holo-RTA in gas phase

Investigation of the vector field representations of gas phase-minimized holo-RTA reveals that the lowest vibrational mode, mode 7 (3.82 cm^{-1}) is similar to the corresponding mode (4.23 cm^{-1}) for apo-RTA, which is a shearing motion between domains I/II and III (Fig. 8). The correlation between these two modes was investigated using the following equation:

$$I_{ab} = \frac{\left| \sum_{i=1}^{3N} a_i b_i \right|}{\left[\sum_{i=1}^{3N} a_i^2 \sum_{i=1}^{3N} b_i^2 \right]^{1/2}} \quad (3)$$

where N is the total number of atoms, and a_i and b_i represent the i th eigenvector components of normal modes a and b , respectively. An I value of 0 indicates two completely uncorrelated modes, whereas an I value of 1 indicates two identical modes. We calculate an I value of 0.77 correlating mode 7 of apo-RTA with the same mode in holo-RTA. This indicates that the shearing motion is not affected

significantly by substrate binding. The minor difference between mode 7 in the differing structures can be attributed to the missing of α -G bending characteristic motion after AMP binding.

However, the above similarity between holo- and apo-RTA is not reproduced in the following normal modes. The breathing motion that dominated the terahertz modes of apo-RTA is found only in modes 10 and 16 of the holo-RTA. Additionally, the upward hinge and α -G bending characteristic motions are significantly reduced in the holo-system. We believe that the breathing motions, and the upward hinge and α -G bending characteristic motions are necessary to facilitate the opening of the active site cleft to allow for the entrance and correct alignment of rRNA, and they are dampened significantly upon substrate binding.

In contrast, the separation between domains I and II at the interface appears more frequently in holo-RTA at modes 8, 9 and 18 (Fig. 8) compared with apo-RTA. Interestingly, this separation motion between domains I and II tends to squeeze the cleft against its back, which will consequently block the rRNA entrance to some extent.

In general, we find that the breathing motion, as well as the upward hinge rising and α -G bending characteristic motions, are dampened significantly upon AMP binding. We hypothesize that these motions contribute to the substrate binding. However, the shearing motion is shared by both apo- and holo-RTA. We propose a hypothesis for this as follows. Fig. 1 demonstrates that most of the functionally important residues (Tyr-80, Tyr-123, Glu-177 and Arg-180) for substrate binding are located in domains I and II but not in domain III. As a result, after AMP binding, domains I and II form an integrated part by the π stacking interaction, but the interaction of AMP with domain III is relatively weak. Since for the shearing motion, domains I and II are moving synchronously along the same direction, the integrity between domains I and II will not be affected significantly by AMP binding. However, the breathing motion involves movement in opposite directions between domains I and II, so this motion will inevitably break the stacking interaction with AMP and hence the integrity of the substrate-bound structure in holo-RTA. This results in the significant dampening in the breathing motion after AMP binding.

4. Conclusions

Terahertz spectroscopy and low frequency normal modes analysis offers a unique probe of the collective low frequency dynamics that are often indicators of conformational changes in proteins. In this work we calculated the terahertz (THz) spectra of apo- and holo- (AMP-bound) A-chain of ricin (RTA), and demonstrated that the low frequency motions were sensitive to substrate binding. This was mainly reflected by the general intensity suppression upon substrate binding. We attribute this intensity suppression to the reduced number of collective motion in THz region, which is consistent with the experimental observations of other proteins. This indicates that THz spectroscopy is expected to offer a unique probe for collective dynamics in such systems. We further carried out the low frequency normal modes analysis of both apo- and holo-RTAs as a means to understand the global motions involved in binding target nucleotide. Based on previous X-ray crystallographic structures of RTA bound with a mono- or dinucleotide substrate analogs, the nucleotide adenine ring is sandwiched between Tyr-80 and Tyr-123 in RTA. As proposed in the introduction, the process of binding and orientating the native rRNA substrate requires flexibility in the protein at the entrance of the active site cleft. A Normal modes analysis confirms the flexibility of the entrance in RTA. We find in the case of the apo-RTA the lowest frequency is a shearing motion, followed by the breathing motions, as well as the upward hinge and the α -G

bending characteristic motions. Except for the shearing motion, these normal modes are dampened in holo-RTA, indicating that the flexibility of the entrance was reduced by AMP binding. In contrast, a separation motion at the interface between domains I and II is more common in holo-RTA. We believe that the breathing, α -G bending and upward hinging motions play an important role in substrate binding as these motions facilitate the entry of the substrate and provide space for the substrate realignment that is necessary for the depurination. Therefore we postulate that inhibitor designs of ricin that are based on analogous of AMP and that can alter these specific low frequency modes (shearing versus breathing) may offer potent inhibitory properties. This analysis casts new light on RTA binding process which is supplemental to the current depurination mechanism [37,39,40].

References

- [1] T.M. Korter, R. Balu, M.B. Campbell, M.C. Beard, S.K. Gregurick, E.J. Heilweil, Terahertz spectroscopy of solid serine and cysteine, *Chem. Phys. Lett.* 418 (2006) 65–70.
- [2] Y. Shi, L. Wang, Collective vibrational spectra of alpha- and gamma-glycine studied by terahertz and Raman spectroscopy, *J. Phys. D: Appl. Phys.* 38 (2005) 3741–3745.
- [3] P.F. Taday, I.V. Bradley, D.D. Arnone, Terahertz pulse spectroscopy of biological materials: L-glutamic acid, *J. Biol. Phys.* 29 (2003) 109–115.
- [4] K. Yamamoto, K. Tominaga, H. Sasakawa, A. Tamura, H. Murakami, H. Ohtake, N. Sarukura, Terahertz time-domain spectroscopy of amino acids and polypeptides, *Biophys. J.* 89 (2005) L22–L24.
- [5] B. Yu, F. Zeng, Y. Yang, Q. Xing, A. Chechin, X. Xin, I. Zeylikovich, R.R. Alfano, Torsional vibrational modes of tryptophan studied by terahertz time-domain spectroscopy, *Biophys. J.* 86 (2004) 1649–1654.
- [6] K. Siegrist, C.R. Buchner, I. Mandelbaum, A.R. Hight-Walker, R. Balu, S.K. Gregurick, D.F. Plusquellic, High-resolution terahertz spectroscopy of crystalline trialanine: extreme sensitivity to beta-sheet structure and co-crystallized water, *J. Am. Chem. Soc.* 128 (2006) 5764–5775.
- [7] S.E. Whitmire, D. Wolpert, A.G. Markelz, J.R. Hillebrecht, J. Galan, R.R. Brige, Protein flexibility and conformational state: a comparison of collective vibrational modes of wild-type and D96N bacteriorhodopsin, *Biophys. J.* 85 (2003) 1269–1277.
- [8] J. Knab, J.-Y. Chen, A.G. Markelz, Hydration dependence of conformational dielectric relaxation of lysozyme, *Biophys. J.* 90 (2006) 2576–2581.
- [9] T. Globus, M. Bykhovskaia, D. Woolard, B. Gelmont, Sub-millimetre wave absorption spectra of artificial RNA molecules, *J. Phys. D: Appl. Phys.* 36 (2003) 1314–1322.
- [10] T. Globus, D. Woolard, M. Bykhovskaia, B. Gelmont, L. Werbos, A.C. Samuels, THz frequency sensing of DNA and related biological materials, *Int. J. High Speed Electron. Syst. (IJHSES)* 13 (2003) 903–936.
- [11] X. Li, A. Bykhovski, B. Gelmont, T. Globus, D. Woolard, M. Bykhovskaia, Computational methods for analysis of terahertz spectral signatures of nucleic acids, *Nanotechnology* 1 (2005) 221–224.
- [12] D. Woolard, T. Globus, B. Gelmont, M. Bykhovskaia, A.C. Samuels, D. Cookmeyer, J.L. Hesler, T.W. Crowe, J.O. Jensen, J.L. Jensen, W.R. Loerop, Submillimeter-wave phonon modes in DNA macromolecules, *Phys. Rev. E* 65 (2002) 051903–051914.
- [13] J. Barber, D.E. Hooks, D.J. Funk, R.D. Averitt, A.J. Taylor, D. Babikov, Temperature-dependent far-infrared spectra of single crystals of high explosives using terahertz time-domain spectroscopy, *J. Phys. Chem. A* 109 (2005) 3501–3505.
- [14] J.F. Federici, B. Schulkin, F. Huang, D. Gary, R. Barat, F. Oliveira, D. Zimdars, THz imaging and sensing for security applications—explosives, weapons and drugs, *Semicond. Sci. Technol.* 20 (2005) S266–S280.
- [15] Y.C. Shen, T. Lo, P.F. Taday, B.E. Cole, W.R. Tribe, M.C. Kemp, Detection and identification of explosives using terahertz pulsed spectroscopic imaging, *Appl. Phys. Lett.* 86 (2005) 24116–24118.
- [16] C.A. Schmuttenmaer, Exploring dynamics in the far-infrared with terahertz spectroscopy, *Chem. Rev.* 104 (2004) 1759–1779.
- [17] P.H. Siegel, Terahertz technology in biology and medicine, *IEEE Trans. Microwave Theory Tech.* 52 (2004) 2438–2447.
- [18] R. Balu, H. Zhang, E. Zukowski, J.-Y. Chen, A.G. Markelz, S.K. Gregurick, Terahertz spectroscopy of bacteriorhodopsin and rhodopsin: similarities and differences, *Biophys. J.* 94 (2008) 3217–3226.
- [19] J.-Y. Chen, J. Knab, J. Cerne, A.G. Markelz, Large oxidation dependence observed in terahertz dielectric response for cytochrome c, *Phys. Rev. E* 72 (2005) 040901.
- [20] J.-Y. Chen, J. Knab, S. Ye, Y. He, A.G. Markelz, Terahertz dielectric assay of solution phase protein binding, *Appl. Phys. Lett.* 90 (2007) 243901.
- [21] A.G. Markelz, J. Knab, J.-Y. Chen, Y. He, Protein dynamical transition in terahertz dielectric response, *Chem. Phys. Lett.* 442 (2007) 413–417.
- [22] A.G. Markelz, S.E. Whitmire, J. Hillebrecht, R. Birge, THz time domain spectroscopy of biomolecular conformational modes, *Phys. Med. Biol.* 47 (2002) 3797–3805.
- [23] E. Castro-Camus, M.B. Johnston, Conformational changes of photoactive yellow protein monitored by terahertz spectroscopy, *Chem. Phys. Lett.* 455 (2008) 289–292.
- [24] H. Yoneyama, M. Yamashita, S. Kasai, K. Kawase, R. Ueno, H. Ito, T. Ouchi, Terahertz spectroscopy of native-conformation and thermally denatured bovine serum albumin (BSA), *Phys. Med. Biol.* 53 (2008) 3543–3549.
- [25] S. Jaaskelainen, C.S. Verma, R. Hubbard, P. Linko, L.S.D. Caves, Conformational change in the activation of lipase: an analysis in terms of low-frequency normal modes, *Protein Sci.* 7 (1998) 1359–1367.
- [26] A.G. Markelz, A. Roitberg, E.J. Heilweil, Pulsed terahertz spectroscopy of DNA, bovine serum albumin and collagen between 0.1 and 2.0 THz, *Chem. Phys. Lett.* 320 (2000) 42–48.
- [27] F. Tama, F.X. Gadea, O. Marques, Y.-H. Sanejouand, Building-block approach for determining low-frequency normal modes of macromolecules, *Proteins Struct. Funct. Genet.* 41 (2000) 1–7.
- [28] F. Tama, Y.-H. Sanejouand, Conformational change of proteins arising from normal mode calculations, *Protein Eng.* 14 (2001) 1–6.
- [29] V. Alexandrov, U. Lehnert, N. Echols, D. Milburn, D. Engelman, M. Gerstein, Normal modes for predicting protein motions: a comprehensive database assessment and associated web tool, *Protein Sci.* 14 (2005) 633–643.
- [30] A. Amadei, A.B.M. Linnsen, H.J.C. Berendsen, Essential dynamics of proteins, *Proteins Struct. Funct. Genet.* 17 (1993) 412–425.
- [31] B.R. Brooks, M. Karplus, Harmonic dynamics of proteins: normal modes and fluctuations in bovine pancreatic trypsin inhibitor, *PNAS* 80 (1983) 6571–6575.
- [32] T. Ichiye, M. Karplus, Collective motions in proteins: a covariance analysis of atomic fluctuations in molecular dynamics and normal mode simulations, *Proteins Struct. Funct. Genet.* 11 (1991) 205–217.
- [33] J. Ma, Usefulness and limitations of normal mode analysis in modeling dynamics of biomolecular complexes, *Structure* 13 (2005) 373–380.
- [34] B.J. Katzin, E.J. Collins, J.D. Robertus, Structure of ricin A-chain at 2.5 Å, *Proteins* 10 (1991) 251–259.
- [35] E. Rutenber, B.J. Katzin, S.R. Ernst, E.J. Collins, D. Misna, M.P. Ready, J.D. Robertus, Crystallographic refinement of ricin at 2.5 Å, *Proteins* 10 (1991) 240–250.
- [36] S.A. Weston, A.D. Tucker, D.R. Thatcher, D.J. Derbyshire, R.A. Pauptit, X-ray structure of recombinant ricin A-chain at 1.8 Å resolution, *J. Mol. Biol.* 244 (1994) 410–422.
- [37] M.A. Olson, Ricin A-Chain structural determinant for binding substrate analogues: a molecular dynamics simulation analysis, *Proteins Struct. Funct. Genet.* 27 (1997) 80–95.
- [38] J.M. Lord, L.M. Roberts, J.D. Robertus, Ricin: structure, mode of action, and some current applications, *FASEB J.* 8 (1994) 201–208.
- [39] A.F. Monzingo, J.D. Robertus, X-ray analysis of substrate analogs in the ricin, *J. Mol. Biol.* 227 (1992) 1136–1145.
- [40] M.P. Ready, Y. Kim, J.D. Robertus, Site directed mutagenesis of ricin A chain and implications for the mechanism of action, *Proteins Struct. Funct. Genet.* 10 (1991) 270–278.
- [41] F. Mentch, D.W. Parkin, V.L. Schramm, Transition-state structures for N-glycoside hydrolysis of AMP by acid and by AMP nucleosidase in the presence and absence of allosteric activator, *Biochemistry* 26 (1987) 921–930.
- [42] Y. Endo, A. Gluck, I.G. Wool, Ribosomal RNA identity elements for ricin A-chain recognition and catalysis, *J. Mol. Biol.* 221 (1991) 193–207.
- [43] C.C. Correll, A. Munishkin, Y.L. Chan, Z. Ren, I.G. Wool, T.A. Steitz, Crystal structure of the ribosomal RNA domain essential for binding elongation factors, *PNAS* 95 (1998) 13436–13441.
- [44] H.A. Heus, A. Pardi, Structure features that give rise to the unusual stability of RNA hairpins containing GNRA loops, *Science* 253 (1991) 191–194.
- [45] B.R. Brooks, D. Janecz, M. Karplus, Harmonic analysis of large systems, *J. Comp. Chem.* 16 (1995) 1522–1542.
- [46] S. Hayward, A. Kitao, N. Go, Harmonic and anharmonic aspects in the dynamics of BPTI: a normal mode analysis and principal component analysis, *Protein Sci.* 3 (1994) 936–943.
- [47] P.J. Day, S.R. Ernst, A.E. Frankel, A.F. Monzingo, J.M. Pascal, M.C. Molina-Svinth, J.D. Robertus, Structure and activity of an active site substitution of ricin A chain, *Biochemistry* 35 (1996) 11098–11103.
- [48] B.R. Brooks, R.E. Bruccoleri, B.D. Olafson, D.J. States, S. Swaminathan, M. Karplus, CHARMM: a program for macromolecular energy, minimization, and dynamics calculations, *J. Comp. Chem.* 4 (1983) 187–217.
- [49] G.M. Day, J.A. Zeitler, W. Jones, T. Rades, P.F. Taday, *J. Phys. Chem. B* 110 (2006) 447–456.
- [50] Y.-H. Sanejouand, Normal-mode analysis suggests important flexibility between the two N-terminal domains of CD4 and supports the hypothesis of a conformational change in CD4 upon HIV binding, *Protein Eng.* 9 (1996) 671–677.
- [51] E.B. Wilson Jr., J.C. Decius, P.C. Cross, *Molecular Vibrations: The Theory of Infrared and Raman Vibrational Spectra*, McGraw-Hill, New York, 1955.
- [52] W. Harrison, Variational calculation of the normal modes of a large macromolecule: methods and some initial results, *Biopolymers* 23 (1984) 2943–2949.
- [53] B.R. Brooks, M. Karplus, Normal modes for specific motions of macromolecules: application to the hinge-bending mode of lysozyme, *PNAS* 82 (1985) 4995–4999.
- [54] O. Marques, Y.-H. Sanejouand, Hinge-bending motion in citrate synthase arising from normal mode calculations, *Proteins Struct. Funct. Genet.* 23 (1995) 557–560.
- [55] A. Thomas, K. Hinsen, M.J. Field, D. Perahia, Tertiary and quaternary conformational changes in aspartate transcarbamylase: a normal mode study, *Proteins Struct. Funct. Genet.* 34 (1999) 96–112.
- [56] W. Humphrey, A. Dalke, K. Schulten, VMD—visual molecular dynamics, *J. Mol. Graph.* 14 (1996) 33–38.
- [57] J.O. Jung, R.B. Gerber, Vibrational wave functions and energy levels of large anharmonic clusters: a vibrational SCF study of (Ar)₁₃, *J. Chem. Phys.* 105 (1996) 10682–10689.